Mesoscopic Simulation of Failure of Mortar and Concrete by 2D RBSM

Kohei Nagai[1], Yasuhiko Sato[2] and Tamon Ueda[3]

Received 29 February 2004, accepted 31 May 2004

Abstract

Concrete is a heterogeneous material consisting of mortar and aggregate at the meso level. Evaluation of the fracture process at this level is useful to clarify the material characteristic of concrete. However, the analytical approach at this level has not yet been sufficiently investigated. In this study, two-dimensional analyses of mortar and concrete are carried out using the Rigid Body Spring Model (RBSM). For the simulation of concrete, constitutive model at the meso scale are developed. Analysis simulates well the failure behavior and the compressive and tensile strength relationship of mortar and concrete under uniaxial and biaxial stress conditions. Localized compressive failure of concrete is also simulated qualitatively.

1. Introduction

The estimation of durability of concrete structures over a long time span that is affected by the various environmental and mechanical loading conditions is an important factor for the efficient and economical construction and maintenance of concrete structures. The study on concrete at the meso level in which concrete consists of mortar and aggregate is useful for the precise evaluation of its material characteristics, which are affected by the material characteristics of the components. Furthermore, the deterioration of the material characteristics of damaged concrete as the result of environmental action can be predicted through analysis at this level in the future (Wittmann 2004).

Much experimental research has been conducted on fracture mechanisms at the meso level in the past. In such research, fracture propagation from the interface between mortar and aggregate to the mortar part is observed in compression tests and the effect of the aggregate on nonlinearity of the macroscopic stress-strain curve of concrete and the failure of concrete are mentioned (Yokomichi et al. 1970, Kosaka and Tanigawa 1975, Trende and Buyukozturk 1998). In recent years, research at the meso level from the analytical point of view has begun but has not been conducted far enough yet. The analysis of compression tests in particular has hardly been carried out due to the complicated failure behavior involved (Nagai et al. 1998, Stroeven and Stroeven 2001, Asai et al. 2003, Bazant et al. 2004). Moreover, the compression and tension strengths relationship of concrete has not been predicted properly through meso scale analysis, which is a necessity basis for the quantitative evaluation of environmental effects on concrete characteristics.

In this study, two-dimensional numerical simulations of failure of mortar and concrete are conducted using the Rigid Body Spring Model (RBSM). This analysis method is useful to simulate discrete behavior like concrete fracture. The authors have conducted research using 2D and 3D RBSM over the past few years (Nagai et al. 2002, 2004) and started to introduce the effect of freeze-thaw action (Ueda et al. 2004). For the simulation of concrete, constitutive models at the meso scale are developed in this study. The fracture process and strength of mortar and concrete under uniaxial and biaxial compression and tension conditions are discussed.

2. Method of numerical analysis

The RBSM developed by Kawai and Takeuchi employs the discrete numerical analysis method (Kawai 1977, Kawai and Takeuchi 1990). Compared with common discrete analysis methods, for example the Distinct Element Method (Cundall and Strack 1979), RBSM is a suitable method for static and small deformation problems. Analyses of concrete or concrete structures with RBSM were conducted by Bolander and Saito (1998) and Ueda et al. (1988).

In RBSM, the analytical model is divided into polyhedron elements whose faces are interconnected by springs. Each element has two transitional and one rotational degree of freedom at the center of gravity. Normal and shear springs are placed at the boundary of the elements **(Fig. 1)**. Since cracks initiate and propagate along the boundary face, the mesh arrangement may affect fracture direction. To avoid the formation of cracks in a certain direction, random geometry is introduced using a Voronoi diagram (**Fig. 2**). A Voronoi diagram is a collection of Voronoi cells. Each cell represents a mortar or

[1]Doctoral course student, Division of Structural and Geotechnical Engineering, Hokkaido University, Japan. *E-mail:* nagai@eng.hokudai.ac.jp
[2]Research Associate, Division of Structural and Geotechnical Engineering, Hokkaido University, Japan.
[3]Professor, Division of Structural and Geotechnical Engineering, Hokkaido University, Japan.

aggregate element in the analysis. For the Voronoi meshing, geometric computational software developed by Sugihara (1998) is applied.

In the nonlinear analysis, a stiffness matrix is constructed on the principle of virtual work (Kawai and Takeuchi 1990), and the Modified Newton-Raphson method is employed for the convergence algorithm. In the convergence process, displacements that cancel the unbalanced force of elements are added to the elements. The displacements are calculated using the stiffness matrix. Convergence of the model is judged when the ratio of summation of squares of unbalanced forces of elements in the model to summation of squares of applied force becomes less than 10^{-5}. When the model does not converge at the given maximum iterative calculation number, analysis proceeds to the next step. The maximum iteration number is set to 400 in this study. The effect of this criterion is discussed in Section 6.4. In the analysis in Chapters 5 and 6, displacement of loading boundary is controlled. The applied strains for one step in analyses are -25×10^{-6} and 2.5×10^{-6} in compression and tension tests, respectively. The simulation program is written in C++ language and the analyses are conducted using a personal computer on Windows.

3. Constitutive model

3.1 Mortar model

In this study, a constitutive model for mortar at the meso level is developed because a constitutive model in the macro scale cannot be applied to meso scale analysis.

The material characteristics of each component are presented by means of modeling springs. In normal springs, compressive and tensile stresses (σ) are developed. Shear springs develop shear stress (τ).

The elastic modulus of springs are presented assuming a plane stress condition,

$$k_n = \frac{E_{elem}}{1-\nu_{elem}^{\ 2}} \qquad k_s = \frac{E_{elem}}{1+\nu_{elem}} \tag{1}$$

where k_n and k_s are the elastic modulus of normal and shear spring, and E_{elem} and v_{elem} are the corrected elastic modulus and Poisson's ratio of component at the meso level, respectively.

In the analysis, due to the original characteristics of RBSM, the values of the material properties at the meso level given to the elements are different from the material properties of the object analyzed at the macroscopic level. In this study, the material properties for the elements were determined in such a way as to give the correct macroscopic properties. For this purpose, the elastic analysis of mortar in compression was carried out. In discrete analysis such as RBSM, the shape and fineness of elements affect analysis results (Nagai 2002). To reduce these effects, a small size for elements is adopted and element fineness in all analyses is maintained to almost the same level. The area of each element in 2D analysis is approximately 2.0~2.5mm in this study. In the elastic analyses, the relationship between the macroscopic and mesoscopic Poisson's ratios and the effect of the mesoscopic Poisson's ratio on the macroscopic elastic modulus were examined. From the results, Eq. (2) and Eq. (3) are adopted for determining the mesoscopic material properties (Nagai et al. 2002).

$$\nu_{elem} = 20\nu^3 - 13.8\nu^2 + 3.8\nu \qquad (0 \leqq \nu \leqq 0.3) \tag{2}$$

$$E_{elem} = (-8\nu_{elem}^{\ 3} + 1.2\nu_{elem}^{\ 2} - 0.2\nu_{elem} + 1)E \tag{3}$$

where E and v are the macroscopic elastic modulus and

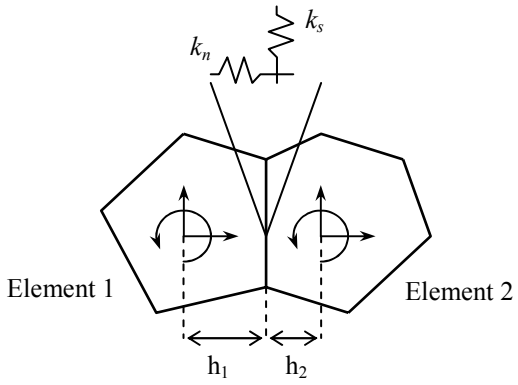

Fig. 1 Mechanical model.

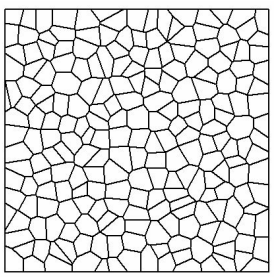

Fig. 2 Voronoi geometry.

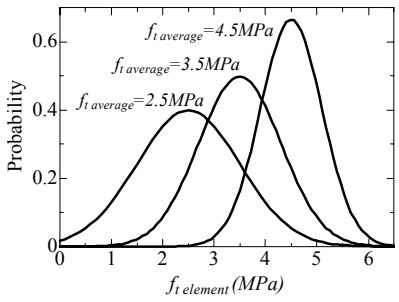

Fig. 3 Distribution of material properties.

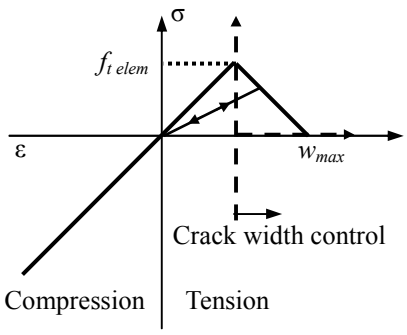

Fig. 4 Model of normal spring.

Poisson's ratio of component of the analyzed object, respectively.

Only the maximum tensile stress has to be set as a material strength. Actually, mortar itself is not a homogeneous material, which consists of sand, paste, air voids, and so on, even when the bleeding effect is ignored. However strength distribution in mortar has not been clarified yet. In this study, a normal distribution is assumed for the tensile strength on the element boundary. The probability density function is as follows (**Fig. 3**),

$$f(ft_{elem}) = \frac{1}{\sqrt{2\pi}\sigma}\exp\left\{-\frac{(ft_{elem}-\mu)^2}{2\sigma^2}\right\}$$
$$\mu = ft_{average} \qquad (4)$$
$$\sigma = -0.2\,ft_{average} + 1.5$$

when $f_{t\,elem} < 0$ then,
$f_{t\,elem} = 0$

where $f_{t\,elem}$ is the distributed tensile strength and $f_{t\,average}$ is the average tensile strength of mortar at the meso level. As seen in Eq. (4) and **Fig. 3**, the distribution varies according to the value of $f_{t\,average}$. This is expressed by stating that higher strength mortar is a more homogeneous material than lower strength mortar. This equation introduces our concept for the general tendency of mortar material properties. The same distribution applies the elastic modulus. These distributions affect the macroscopic elastic modulus, so that the elastic modulus for the element is multiplied by 1.05.

Springs set on the face behave elastically until stresses reach the τ_{max} criterion or tensile strength. The strains and stresses are calculated as follows.

$$\varepsilon = \frac{\Delta n}{h_1 + h_2}$$
$$\gamma = \frac{\Delta s}{h_1 + h_2} \qquad (5)$$
$$\sigma = k_n \varepsilon$$
$$\tau = k_s \gamma$$

where ε and γ are the strain of normal and shear springs, respectively. Δn and Δs are the normal and shear relative displacement of elements of those springs, respectively. h is the length of the perpendicular line from the center of gravity of element to the boundary, and subscripts 1 and 2 represent elements 1 and 2 in **Fig. 1**, respectively.

The constitutive model of a normal spring is shown in **Figure 4.** In the compression zone, such a spring always behaves elastically. Fracture happens between elements when the normal spring reaches tensile strength $f_{t\,elem}$, and the normal stress decreases linearly depending on the crack width, which corresponds to the spring elongation. In this study, w_{max} is set 0.03 mm, which expresses more brittle behavior than the general macro scale concrete model. The linear unloading and reloading path that goes through the origin is introduced to the normal spring in the tension zone. For shear springs, an elasto plastic model is applied as shown in **Fig. 5** in the range where normal springs do not fracture. The value of τ_{max} changes depending on the condition of the normal spring and is given as follows (**Fig. 6**),

$$\tau_{\max} = \pm(0.11 f_{telem}{}^{3.0}(-\sigma + f_{telem})^{0.6} + f_{telem}) \quad (\sigma \leqq f_{telem}) \qquad (6)$$

This criterion and the value of τ_{max} are originally developed for 2D RBSM meso-scale analysis. It has been confirmed that they considerably affect the results of analysis.

When fracture occurs in the normal spring, the calculated shear stress is reduced according to the reduction ratio of normal stress. As a result, the shear spring cannot carry the stress when the crack width of the normal spring reaches w_{max}.

After the stresses reach the criterion, the stresses are carried only through a wrapped part on the boundary to shear direction, which is calculated by the elongation of the shear spring and the length of the boundary where the springs are set.

In the constitutive model, normal springs in compression only behave elastically and never break nor exhibit softening behavior.

3.2 Aggregate model

In this study, the effect of the existence of aggregate in concrete on the fracture process is examined. For this purpose, aggregate elements behave only elastically without fracture in this study. The same equations as (1), (2), (3) and (5) are adopted to present the material prop-

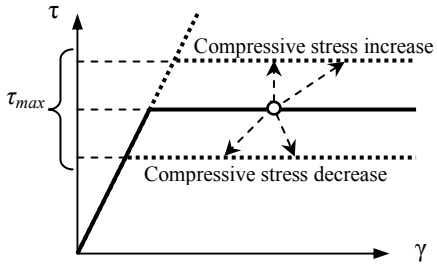

Fig. 5 Model of shear spring.

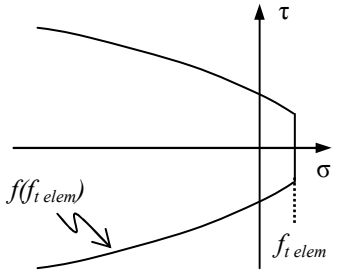

Fig. 6 τ_{max} criterion for mortar.

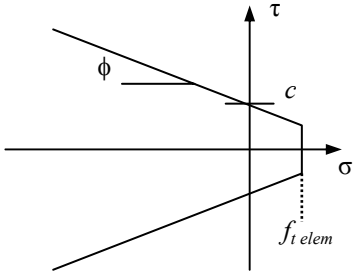

Fig. 7 τ_{max} criterion for interface.

erty of aggregate.

3.3 Interface model

The same stress strain relationships as Eq. (5) and strength and stiffness distribution as Eq. (4) are adopted for the material properties of the interface between the mortar and aggregate. The spring stiffnesses k_n and k_s of the interface are given by a weighted average of the material properties in two elements according to their perpendiculars, i.e.,

$$k_n = \frac{k_{n1}h_1 + k_{n2}h_2}{h_1 + h_2}$$
$$k_s = \frac{k_{s1}h_1 + k_{s2}h_2}{h_1 + h_2} \quad (7)$$

where subscripts 1 and 2 represent elements 1 and 2 in **Fig. 1**, respectively.

Similar constitutive models of the spring between mortars are applied to the interface springs. For the normal spring, the constitutive model in **Fig. 4** is adopted. For the interface spring, w_{max} is set 0.01 mm. For shear springs, an elastoplastic model as shown in **Fig. 5** is applied. The τ_{max} criterion for the interface as shown in Eq. (8) and **Fig. 7** is adopted.

$$\tau_{\max} = \pm(-\sigma \tan\phi + c) \qquad (\sigma \leqq f_{telem}) \quad (8)$$

where ϕ and c are constant values. This criterion is based on the failure criterion suggested by Taylor and Broms (1964) and Kosaka et al. (1975), which is derived from experimental results. Similarly to the spring between mortars, when fracture happens in normal spring, the calculated shear stress is reduced according to the reduction ratio of normal stress.

Similarly to the mortar model, stresses are carried only through a wrapped part on the boundary to shear direction after the stresses reach the τ_{max} criterion.

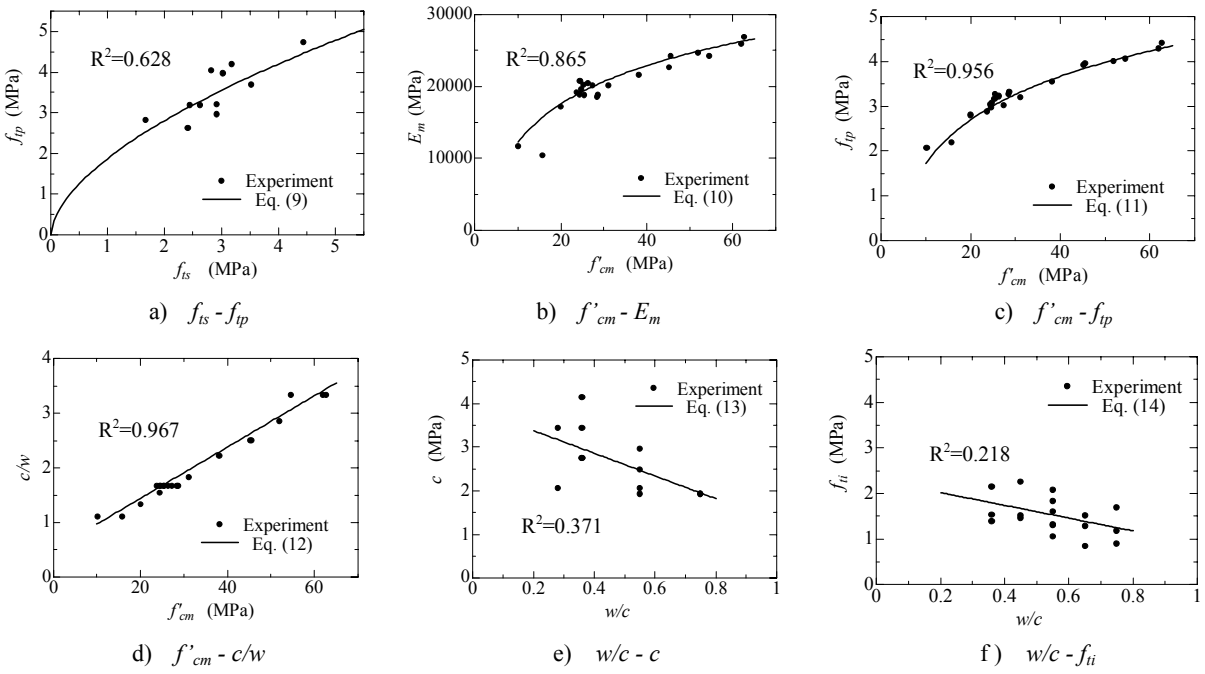

Fig. 8 Relationships of material properties.

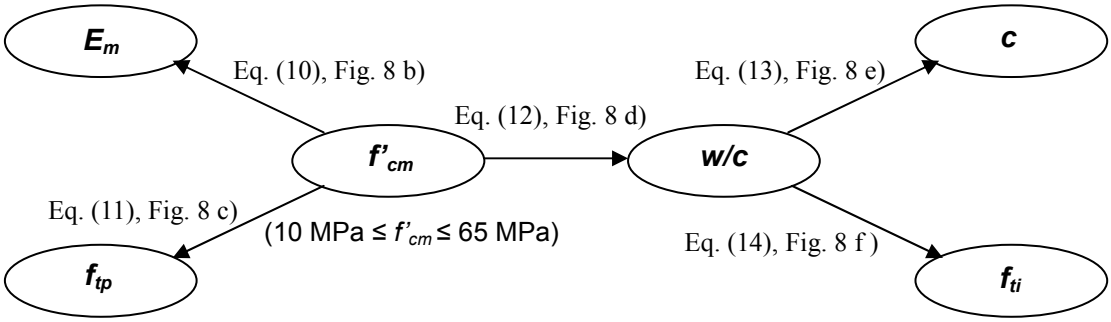

Fig. 9 Flowchart for determination of input material properties.

4. Input material properties

In this study, numerical simulation of failure of normal concrete is carried out. For the simulation, the material properties of mortar, aggregate and interface between mortar and aggregate have to be introduced as input data (see Chapter 3). Some values of these material properties are not independent but affect each other, and therefore a method for determining the input material properties is developed based on a previous experiment. However, the sizes of the specimens in the experiment referred to in this study are not the same level as that of the element in the simulation. This indicates that further experimental research at the meso level should be carried out in the future for the development of more accurate meso-scale analytical material modeling

The experimental research conducted by Hsu and Slate (1963), Taylor and Broms (1964), Kosaka et al. (1975) and Yoshimoto et al. (1983) are referred to in order to examine the relationship between compressive strength of mortar (f'_{cm}), elastic modulus of mortar (E_m), pure tensile strength of mortar (f_{tp}), splitting tensile strength of mortar (f_{ts}), water cement ratio (w/c or c/w), value of c in the τ_{max} criterion for interface (see Eq. (8) and **Fig. 7**) and tensile strength of interface (f_{ti}). **Fig. 8 a**) shows results of the experiment on the relationship between pure tensile strength (f_{tp}) and splitting tensile strength (f_{ts}) conducted by Yoshimoto et al. (1983). Based on these results, the following relationship is adopted.

$$f_{tp} = 1.88 f_{ts}^{0.58} \tag{9}$$

Kosaka et al. (1975) carried out experiments on the interface failure criterion. From the measured mortar material properties, equations to present the relationship between f'_{cm} and E_m (**Fig. 8 b**)), f'_{cm} and f_{tp} (**Fig. 8 c**)) and f'_{cm} and c/w (**Fig. 8 d**)) are developed, where splitting tensile strength (f_{ts}) in the experiment is modified to pure tensile strength (f_{tp}) using Eq. (9). These relationships are,

$$E_m = 1000\{7.7 Ln(f'_{cm}) - 5.5\} \tag{10}$$

$$f_{tp} = 1.4 Ln(f'_{cm}) - 1.5 \tag{11}$$

$$c/w = 0.047 f'_{cm} + 0.5 \tag{12}$$

where the data of compressive strength of mortar from 10MPa to 65MPa are applied. Equations to present the c-w/c and f_{ti}-w/c relations are developed based on the experiments conducted by Hsu and Slate (1963) and Taylor and Broms (1964), respectively (**Fig. 8 e**) and (**Fig. 8 f**). Differences in aggregate types and cement-sand ratios in mortar are not taken into consideration. The equations are as follows.

$$c = -2.6 w/c + 3.9 \tag{13}$$

$$f_{ti} = -1.44 w/c + 2.3 \tag{14}$$

Figure 9 shows the developed flowchart for determination of input material properties relationships Eq. (10) to Eq. (14). Using the flowchart, the necessary material properties for the simulation, E_m, f_{tp}, c and f_{ti}, can be calculated from the target compressive strength of mortar (f'_{cm}). However the value of f'_{cm} itself is not introduced in the simulation (see Chapter 3). The tensile strengths of mortar (f_{tp}) and interface (f_{ti}) calculated in this chapter are applied as the average tensile strength ($f_{t\,average}$) of the component at the meso level in Chapter 3.

In addition, the elastic modulus of aggregate (E_a), Poisson's ratio of mortar (v_m) and aggregate (v_a) and ϕ for the interface τ_{max} criterion must be introduced in the simulation. Sufficient research on the values of E_a, v_m and v_a has not yet been carried out, and therefore the general values of 50 GPa, 0.18 and 0.25, respectively, are adopted in all simulations. Regarding the value of ϕ, due to the difficulty of clarifying the quantitative relationship from the previous studies (Taylor and Broms 1964, Kosaka et al. 1975), a typical value of 35° is applied to all the simulations.

5. Analysis of mortar

5.1 Compression and tension test

Numerical analysis of mortar specimens in uniaxial compression and tension are carried out. **Figure 10** shows an analyzed specimen. The size of the specimen is 100 × 200 mm and the number of elements is 3,200. The top and bottom loading boundaries are fixed in the lateral direction in the compression test and are not fixed in the tensile test. The target compressive strength of mortar is 35 MPa, so that the input material properties in simulation are calculated as shown in **Table 1** using the flowchart for determining input material properties (see Chapter 4). **Fig. 11** shows the predicted stress strain curve in the compression test. Lateral strain is calculated by the relative deformation between the elements at A and B in **Fig. 10.** The strength of the specimen is 36.02 MPa. The target macroscopic compressive strength of the specimen is predicted well by the simulation in which only tensile and shear failures are allowed on the meso scale. Predicted curves in compression show nonlinearity in the axial direction before 50% of maximum stress. The ratio of the lateral strain to the axial strain starts increasing rapidly around 70% of maximum stress. These behaviors were also observed in mortar compression test experiments (Harsh et al. 1990, Globe and Cohen 1999). **Figure 12** shows the deformation of a specimen at axial strain of $-3{,}000\times10^{-6}$. The deformation is enlarged 10 times. Macro shear cracking observed in usual experiments is simulated. The macro shear cracks emerge around the peak stress and propagate steadily to the failure.

The predicted stress strain curve in tension analysis is presented in **Fig. 13.** The macroscopic tensile strength of the specimen is 3.48 MPa, which also agrees well with the given strength in tension (see **Table 1**). The

shape of the stress strain curve shows nonlinearity before the peak stress as much as in compression. This behavior was observed in experiments of pure tensile testing of mortar (Gopalaratnam and Shah 1985). **Figure 14** shows the deformation of the model at failure. The deformation is enlarged 50 times. Propagation of single crack that can be seen in usual experiments can be simulated. **Fig. 15** shows the average strains of every 50 mm section in the axial direction. To calculate the strains of *0-50 mm*, *50-100 mm*, *100-150 mm* and *150-200 mm* in **Fig. 15**, relative deformations between the elements at C and D, D and E, E and F and F and G, respectively, in **Fig. 10** are used. The vertical axis shows the macroscopic stress. Until the peak, similar curves are predicted. This means that the model elongates uniformly. In the post peak range, only the strain in the *50-100 mm* range, where the single crack propagates (see **Fig. 14**) increases and the strains in other sections decreases. This localization behavior in failure processes in tension is also observed in usual experimental results.

Table 1 Input material properties of mortar.

$f_{t\,average}$	3.48 MPa
Elastic modulus (E_m)	21,876 MPa
Poisson's Ratio (v_m)	0.18

5.2 Variation in strength of mortar

The simulated results of the test vary due to the fact that the random element meshing and the strength and stiffness distribution in the specimens were provided separately (see Chapter 3) even when the specimen size and the fineness of the elements were the same. To examine this variation, compression and tension tests of mortar are carried out in three target compressive strength cases, 15 MPa, 35 MPa and 55 MPa. The size of the model is 100 × 200 mm and the number of elements is 3,200. The loading boundaries are fixed in the lateral direction in compression tests and are not fixed in tension tests.

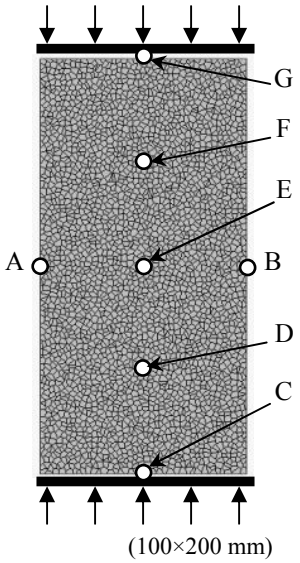

Fig. 10 Mortar specimen.

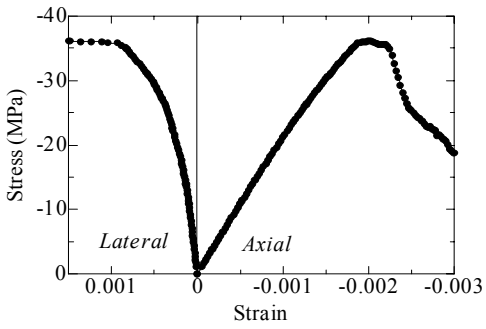

Fig. 11 Stress strain curve in compression.

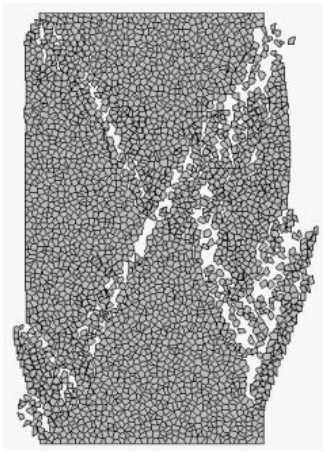

Deformation × 10

Fig. 12 Failure in compression.

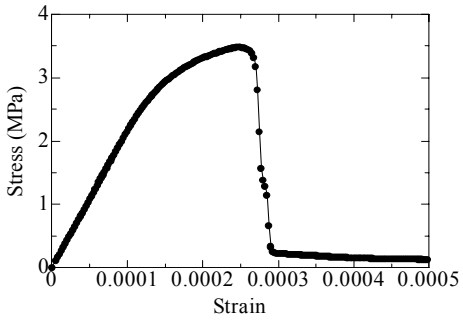

Fig. 13 Stress strain curve in tension.

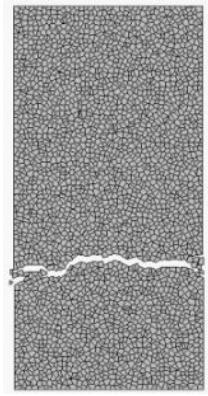

Deformation × 50

Fig. 14 Failure in tension.

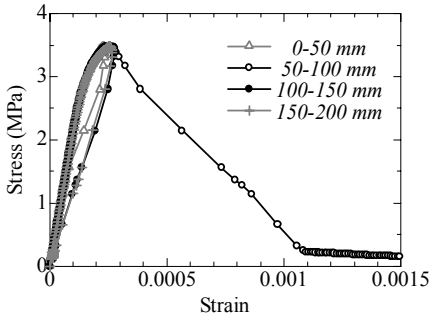

Fig. 15 Strain in every 50mm in axial direction.

Table 2 Variation of strength of mortar.

Target f'_{cm} (set $f_{t\,average}$)	Compression			Tension		
	Ave. f'_{cm}	SV	CV	Ave. f_{tm}	SV	CV
15MPa (2.29MPa)	13.35MPa	0.330MPa	2.47%	2.10MPa	0.072MPa	3.44%
35MPa (3.48MPa)	35.41MPa	1.367MPa	3.86%	3.45MPa	0.108MPa	3.15%
55MPa (4.11MPa)	56.56MPa	3.275MPa	5.79%	4.23MPa	0.134MPa	3.30%

SV: Standard variation, CV: Coefficient of variation.

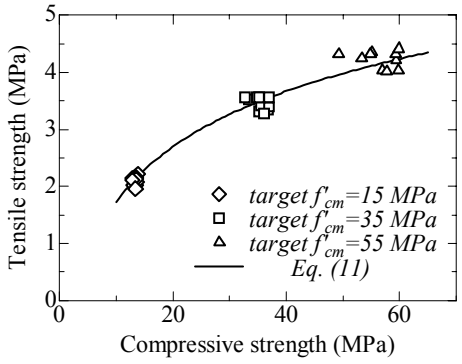

Fig. 16 Compressive-tensile strength relationship.

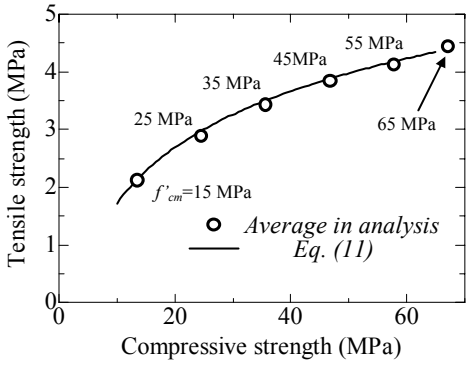

Fig. 17 Average strength relationship of mortar.

Those conditions are the same as for the simulations in Section 5.1. For each target compressive strength of the mortar, simulations of 10 specimens where element meshing and the strength and stiffness distribution in the model are given separately are conducted.

In the analyses of each target compressive strength, the stress strain curves in all specimens are on the same line until around the peak stress. They show a different peak stress as a result of the different element meshing and strength and stiffness distribution in the specimen. Crack patterns at failure are similar in all simulations and are as shown in **Figs. 12** and **14**. Though similar behaviors are simulated in all target compressive strength cases, variation in strength becomes larger at higher mortar strength, as shown in **Fig. 16**, where compressive and tensile strength relationships in the simulation are presented. **Table 2** shows the average strength, the standard variation in strength and the coefficient of variation in strength in the analysis. The average strengths of specimens agree well with the target compressive strengths and set average tensile strengths. In compression, though the variation in material properties on the meso scale become smaller (see Eq. (4) and **Fig. 3**), the coefficient of variation increases with high strength. In the statistical research on the variation in mortar strength based on experiments, the coefficient of variation does not change with strength in compression and bending tests and the value is approximately 2 to 4% in compression (Nagamatsu 1976). Analysis predicts a slightly higher value in high strength in compression.

5.3 Relationship of strength in compression and tension

Analyses of uniaxial compression and tension test of mortar are carried out to examine the relationship between compressive and tensile strength. The size of the model, number of elements and boundary condition are the same as in the analyses in Section 5.2. Target compressive strengths are set in 10 MPa increments from 15 MPa to 65 MPa. For each target strength, compression and tension analyses on 5 specimens are conducted because average strength becomes almost constant when more than 5 data are obtained by the analysis in Section 5.2. The results include the analyses in Section 5.2. **Figure 17** shows the predicted average strength relationship of mortar. The analysis can simulate the strength relationship well although only the tensile strength is given as the material strength in the analysis.

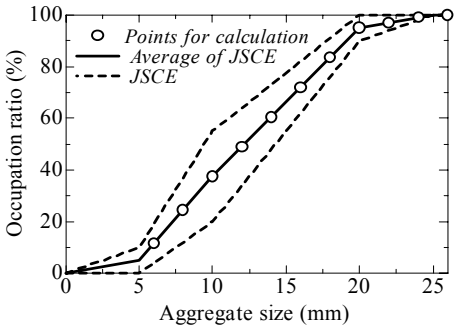

Fig. 18 Grain size distribution.

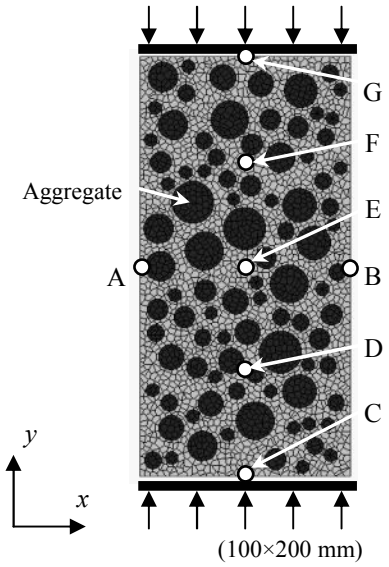

Fig. 19 Concrete specimen.

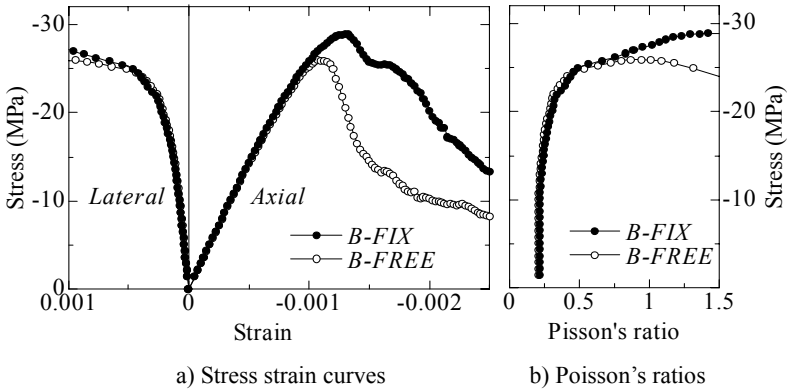

a) Stress strain curves b) Poisson's ratios

Fig. 20 Stress strain curves and Poisson's ratios.

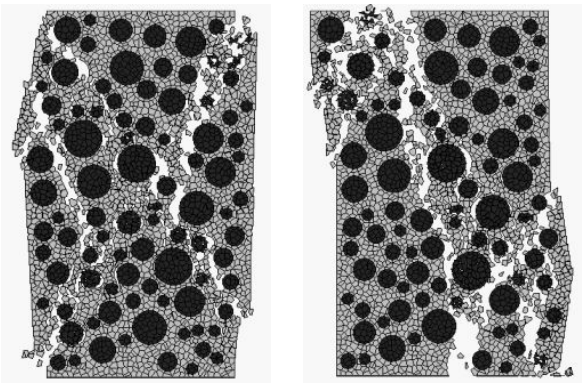

a) B-FIX b) B-FREE

Deformation × 10

Fig. 21 Failure in compression.

6. Analysis of uniaxial test of concrete

Numerical analyses of failure of concrete under uniaxial compression and tension are carried out in this section. The shape of the coarse aggregate in the concrete is circular. The effect of the shape of aggregate will be studied in the future. Aggregate size distribution is determined based on the JSCE Standard Specification for Concrete Structures (2002a) and the maximum aggregate size is 20 mm as shown in **Fig. 18**. Aggregate diameters used for the analysis are varied at 2 mm increments. The number of the aggregates of each size is calculated using the distribution curve in **Fig. 18** and the points on the curve indicate the selected diameters. The volume of the aggregate is approximately 38%, which is similar to that of usual concrete, and these aggregates are introduced randomly in the specimen.

6.1 Compression and tension test

Compression and tension analysis of concrete are carried out. **Figure 19** shows a specimen where the number of elements is 3,619 including 1,619 elements of aggregate. In the compression analyses, 2 types of models are analyzed: (i) Model where the top and bottom boundaries are fixed in the lateral direction (B-FIX); and (ii) Model where the boundaries are not fixed in the lateral direction (B-FREE). The effect of loading boundary condition in the compression test in an experiment was extensively discussed by Kotsovos (1983) for the first time. In the tension test, the loading boundaries in the lateral direction are not fixed. The target compressive strength of mortar is set to 35 MPa and the input material properties are calculated by the flowchart in **Fig. 9**.

Figure 20 shows the predicted curves of stress-strain and stress-Poisson's ratio of specimens B-FIX and B-FREE. To calculate the lateral strain, the relative deformation between points at A and B in **Fig. 19** is used. The macroscopic strengths are 28.91MPa and 25.82MPa for specimens B-FIX and B-FREE, respectively. The natures of the curves are similar to those mentioned by Kosaka and Tanigawa (1975a). A slight reduction in macroscopic strength due to the elimination of friction on the loading boundary is observed in the analysis, similarly to the experiment (Kosaka and Tanigawa 1969, Kosaka and Tanigawa 1975a, Matsushita et al. 1999). **Figure 20 b**) shows the changes in Poisson's ratio. Until approximately 25MPa, the curves of specimens B-FIX and B-FREE agree well. However from the point that Poisson's ratio increases rapidly, macroscopic stress of specimen B-FIX increases and specimen B-FREE fails because the loading boundary of specimen B-FREE cannot restrict the expansion of the specimen in the lateral direction. This behavior is observed in the experiment and mentioned by Kosaka and Tanigawa (1975a). Failure deformations of the specimens are shown in **Fig. 21** (at axial strain of $-2{,}500\times10^{-6}$). The shear crack forming triangle zone on the boundary in specimen B-FIX and the longitudinal main cracks reaching the

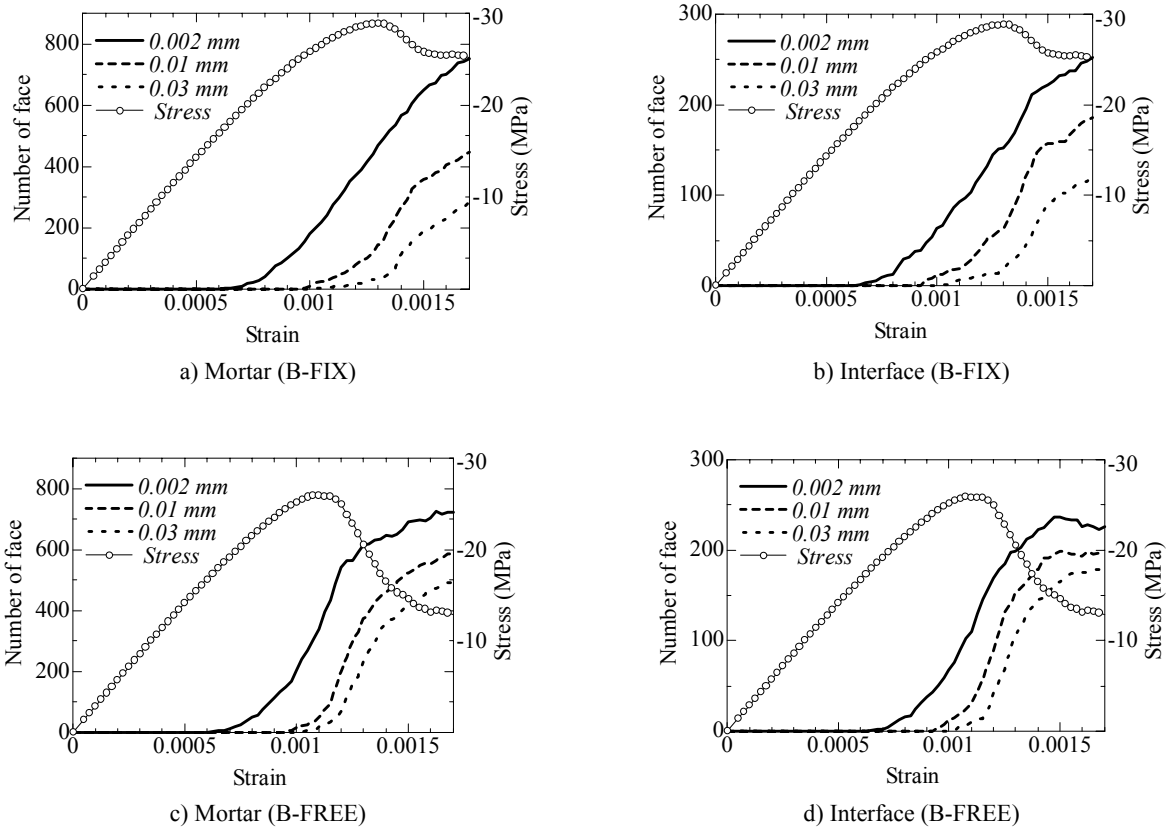

Fig. 22 Number of faces reaching certain crack width.

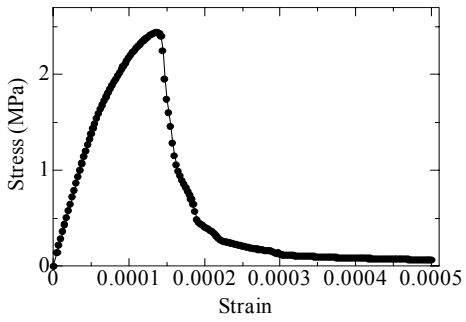

Fig. 23 Stress strain curve in tension.

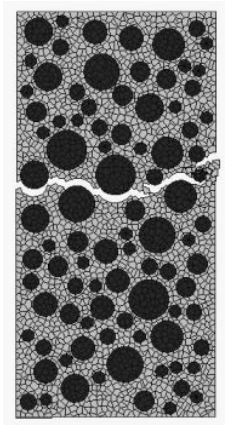

Fig. 24 Failure in tension.

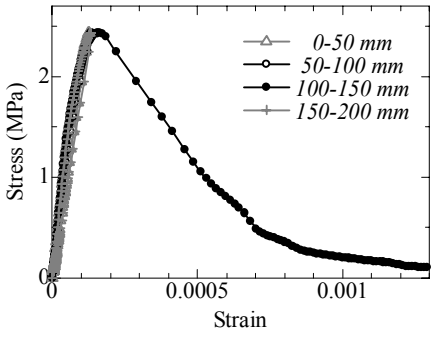

Fig. 25 Strain at every 50 mm in axial direction.

loading boundary in specimen B-FREE are predicted. This difference in crack pattern is observed in the experiment (Matsushita et al. 1999). The curves in **Fig. 22** show the numbers of faces where springs are set in mortar and the interfaces where the crack width reaches 0.002 mm, 0.01 mm and 0.03 mm in specimens B-FIX and B-FREE. Horizontal axes show the macroscopic strain of specimens. The macroscopic stresses of the specimens are presented in the graphs. Both specimens fail after the rapid increase in mortar and interface cracks. This is similar to the usual experimental results (Kato 1971, Kosaka and Tanigawa 1975b). The increase in the number of cracks reaching a certain crack width around the peak stress is more rapid in specimen B-FREE than in specimen B-FIX. This indicates that rapid propagation of cracks takes place in specimen B-FREE as the result of the free loading boundary. This behavior is mentioned experimentally by Kotsovos (1983).

Figure 23 shows the predicted stress strain curve in

Table 3 Variation of strength of concrete.

Target f'_{cm} (set $f_{t\,average}$)	Compression			Tension		
	Ave. f'_c	SV	CV	Ave. f_{tcp}	SV	CV
25MPa (3.01MPa)	21.28MPa	0.686MPa	3.22%	2.12MPa	0.074MPa	3.52%
45MPa (3.83MPa)	35.23MPa	1.886MPa	5.35%	2.70MPa	0.105MPa	3.87%
65MPa (4.34MPa)	45.62MPa	3.820MPa	8.37%	3.04MPa	0.145MPa	4.77%

SV: Standard variation, CV: Coefficient of variation.

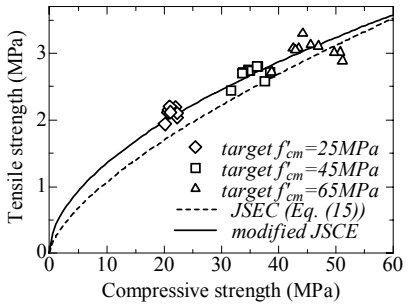

Fig. 26 Compressive-tensile strength relationship.

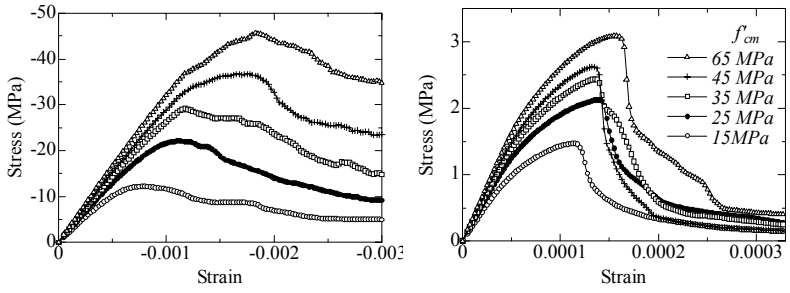

a) Compression b) Tension

Fig. 27 Results of compression and tension tests.

the tension test. The strength of the specimen is 2.44 MPa. The nonlinearity in predicted stress strain curve before the peak stress is observed in the pure tensile test in the experiment (Gopalaratnam and Shah 1985, Ueda et al. 1993). Deformation of the model at failure is presented in **Fig. 24** (at axial strain of 400×10^{-6}). The deformation is enlarged 50 times. The propagation of single cracks that can be seen in usual experiments can be simulated (Ueda et al. 1993). **Figure 25** shows the average strains of every 50 mm section in the axial direction. To calculate the strains of *0-50 mm*, *50-100 mm*, *100-150 mm* and *150-200 mm* in **Fig. 25**, the same calculation method as in Section 5.1 is adopted. The vertical axis shows the macroscopic stress. Similar curves to those in mortar analysis are predicted until the peak. In the post peak range, only the strain in the *100-150 mm* range, where the single crack propagates (see **Fig. 24**) increases and the strains in other sections decrease. This localization behavior in failure processes in tension is also measured in the experiment (Gopalaratnam and Shah 1985).

6.2 Variation in strength of concrete

Same as the case of mortar, variation in strength of concrete is examined in this section (see Section 5.2). The target compressive strengths of mortar are 25 MPa, 45 MPa and 65 MPa, respectively. For each target strength, uniaxial compression and tension tests of 10 specimens where the location of aggregates, the element meshing and the strength and stiffness distribution in the specimen are different are conducted. The numbers of elements in all the specimens is approximately 3,650. The loading boundaries are fixed in the lateral direction in

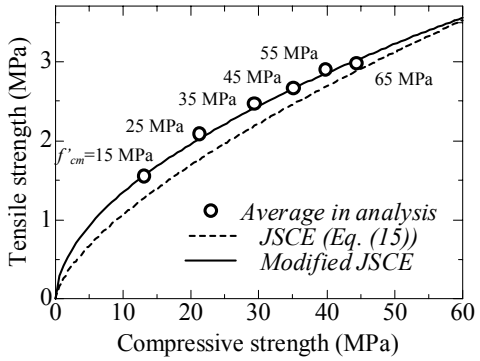

Fig. 28 Average strength relationship of concrete.

compression tests and are not fixed in tension tests. Input material properties are determined by the developed flowchart in **Fig. 9.**

Figure 26 shows the compressive and tensile strength relationship in simulations. The curve in the graph shows the strength relationship suggested by JSCE (2002b). This relationship is,

$$f_{tcs} = 0.23 f'^{\,2/3}_{c} \tag{15}$$

where f'_c and f_{tcs} are the compressive and splitting tensile strength of concrete, respectively. In the analysis, pure tensile tests are carried out, and therefore Eq. (15) is modified by the equation developed by Yoshimoto et al. (1983) for pure tensile strength that is presented in **Fig. 26. Table 3** shows the predicted average strength, standard variation in strength and coefficient of variation in strength. In both compression and tension tests,

reductions in average strengths of concrete due to the introduction of aggregates in mortar observed in experiment are predicted (Christensen and Nielsen 1969, Kosaka et al. 1975, Stock et al. 1979). The coefficient of variation increases with strength. In the experiment, the coefficient of variation in strength of concrete does not change with strength (Nagamatsu 1967, Suzuki et al. 2003). Although the value of the coefficient of variation increases with strength in analyses, the values are less than 10%.

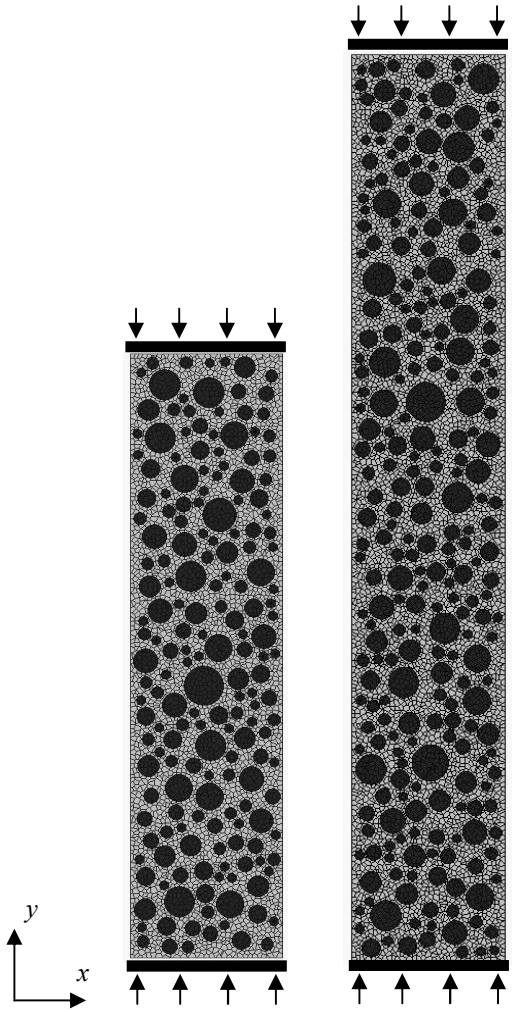

Fig. 29 View of specimens.

6.3 Relationship of strength in compression and tension

The relationship between the compressive and tensile strength of concrete is examined. In this study, the relationships are examined using the results of average values obtained from 5 data for each target compressive strength of mortar because the difference of average strengths become small enough, i.e. less than 10%, when more than 5 data are obtained. The target compressive strength of mortar is set in 10 MPa increments from 15MPa to 65MPa. The number of element in the specimens is approximately 3,650. The results in Section 6.2 are included in this data. The stress strain curves in **Fig. 27** show some of the results of the compression and tension tests conducted in this section. **Figure 28** shows the predicted results of relationship of average strength. The predicted compression and tension strength relationship of concrete agrees well with the experimental relationship. The applicable compressive strength of concrete in this analysis ranges approximately from 10 MPa to 45 MPa.

6.4 Analysis of localized failure in compression

It is known that the localization of failure is observed in the compression failure of concrete (Mier 1986, Markeset and Hillerborg 1995, Watanabe et al. 2003). The localization is observed in the post peak region. In this section, compression tests of concrete specimens where the height-width ratios of specimens (H/D) are 4.0 and 6.0 are carried out to simulate failure localization. The widths of the specimens are 100 mm and the height is 400 mm in specimen H400 and 600 mm in specimen H600. **Figure 29** shows the view of specimens. The numbers of elements are 6,618 and 9,826 in specimens H400 and H600, respectively. The target compression strength of mortar is 35 MPa. Loading boundaries are not fixed in the lateral direction. Analysis proceeds until the macroscopic stress is reduced to approximately 25% of peak stress.

As mentioned in Chapter 2, analysis proceeds to the

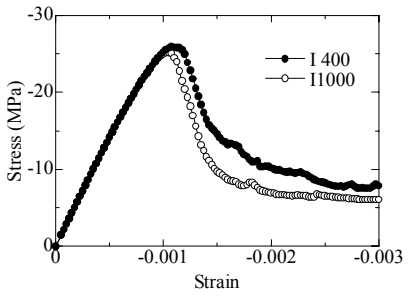

Fig. 30 Stress strain curves of specimen B-FREE.

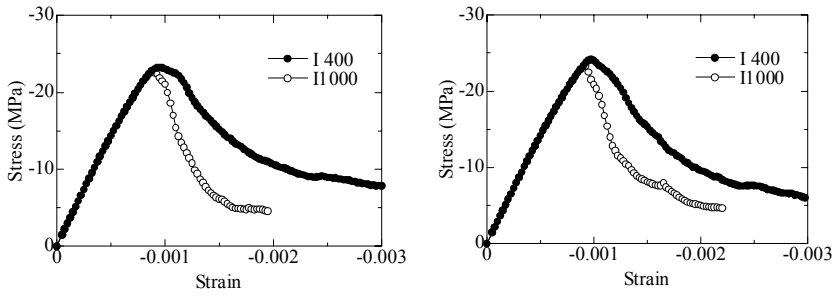

a) Specimen H400 b) Specimen H600

Fig. 31 Stress strain curves.

next step when the model does not converge at 400 iterations in the RBSM analysis in which the Modified Newton-Raphson method is employed for the convergence algorithm. The authors have confirmed that the criterion affects the result of analysis in the post peak range. **Figure 30** shows the effect of the calculation of the maximum iteration number in the compression test of specimen B-FREE in Section 6.1 where two maximum iteration numbers are applied: 400 times (I400) and 1,000 times (I1000). Different stress strain curves are observed in the post peak range because the analysis cannot reach the allowable level of the unbalanced force in the specimen. However the behavior until the peak stress and the location of the major crack in the post peak range are almost same. This difference becomes big in the analyses of specimens H400 and H600. **Figure 31** shows the predicted stress strain curves where criteria I400 and I1000 are applied. For both criteria, the significant difference in the macroscopic stress strain curve caused by specimen height observed in the experiment cannot be simulated (Watanabe et al. 2003).

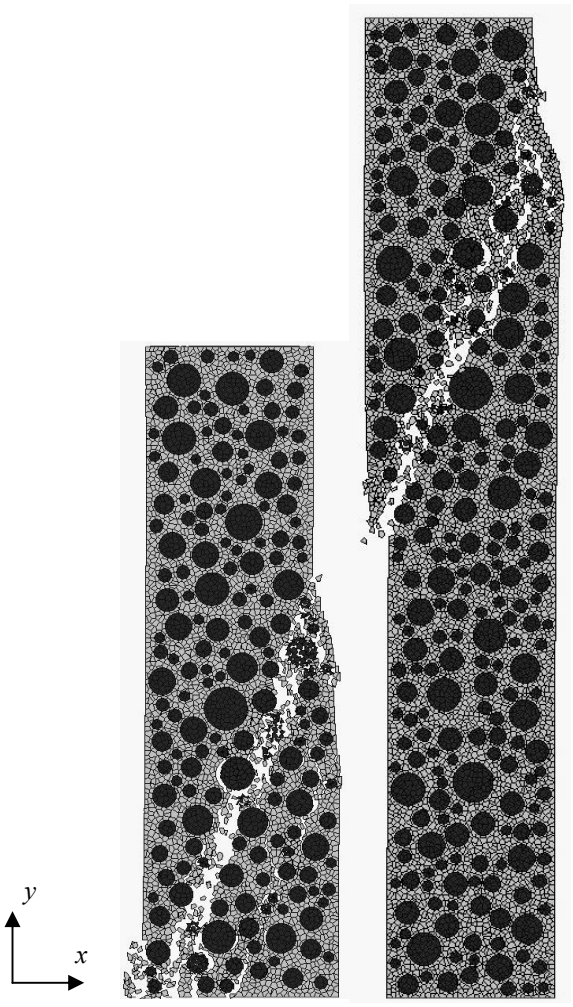

a) H400-I400 b) H600-I400

Deformation × 10

Fig. 32 Failure deformations.

These criteria suggest the issues to be solved in future research with regard to the nonlinear analysis in the post peak range adopted by this study.

However, the stress strain curves until the peak stress are similar in each specimen and the strengths are 23.01MPa in specimen H400 and 24.14MPa in specimen H600 in analyses of the I400 series. The strength of specimen B-FREE in Section 6.1 is 25.82 MPa, where the height of the specimen is 200 mm. The fact that the compressive strength does not change with the height of the model is similar to experimental observations in previous studies (Matsushita et al. 1999, Watanabe et al. 2003).

The failure deformations of specimens in the analyses

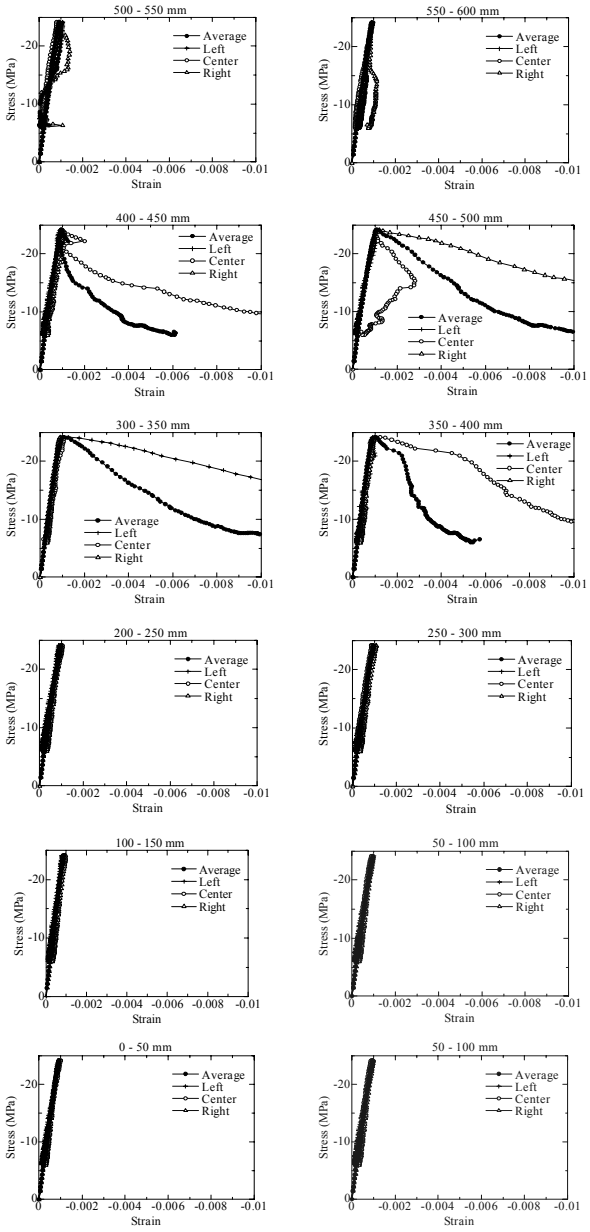

Fig. 33 Strain in every 50mm in axial direction (H600-I400).

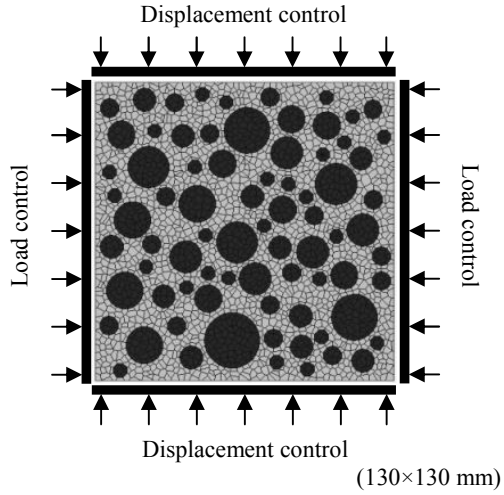

Fig. 34 Numerical specimen for biaxial test.

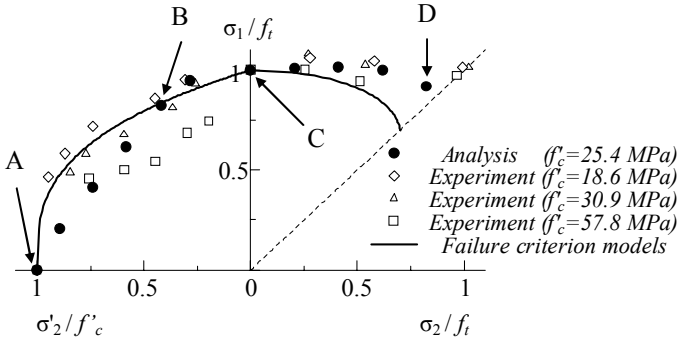

Fig. 35 Failure criterion under biaxial stress.

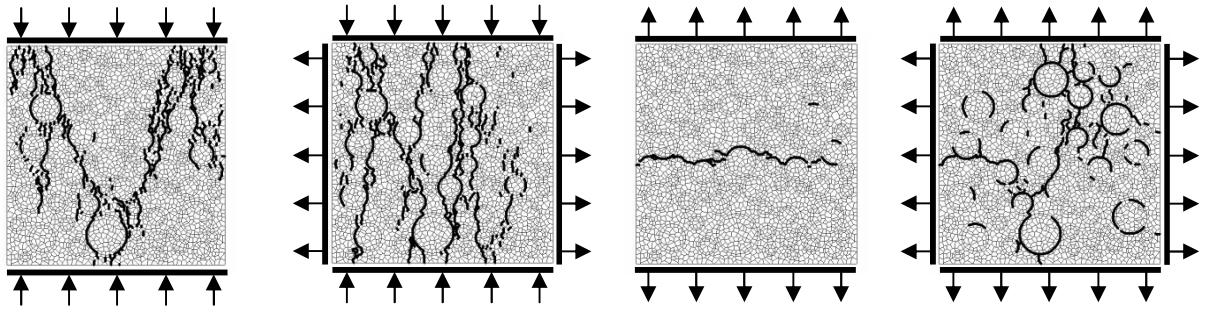

a) Point at A b) Point at B c) Point at C d) Point at D

Fig. 36 Crack patterns.

of the I400 series are shown in **Fig. 32** (at axial strain of approximately $-1{,}600\times10^{-6}$). Although the fracture spreads more widely around a major crack in the analyses of the I400 series compared with the I1000 series, the locations of the major crack in both series are quite similar. In all analyses, a failure zone of approximately 250 mm height is observed. **Figure 33** shows the local strain of every 50 mm section in the axial direction in the I400 series of specimen H600. Local strain is calculated in the same way as in Sections 5.1 and 6.1. For each section, three strains are calculated at the left side (at x=13.6 mm), center (at x=50 mm), and right (at x=83.6 mm) because the strain varies considerably depending on the location of the major shear crack. The averages of the three strains are also shown in the figures. The vertical axis shows the macroscopic stress. Strains in the 0 mm-300 mm section do not increase after the peak stress but show unloading behavior where no major crack is observed. In contrast, the strains in the 300 mm-500 mm section show an increase in the post peak region where the major shear crack occurs (see **Fig. 32**). In the experiment by Watanabe et al. (2003), the size of the localized compressive failure zone is estimated at 100-140 mm for the 100 mm width specimen and the unloading behavior is measured in other parts. Except for the fact that the analysis predicts the failure zone with a double size, the behavior in compression failure of concrete can be simulated well. In other simulations conducted in this section, similar localized compressive failures are observed.

7. Analysis of biaxial test of concrete

Numerical simulations of failure of concrete under biaxial loading condition are carried out in this chapter. **Figure 34** shows the specimen for the simulation. The size of the model is 130 × 130 mm and the number of elements is 3,353. The aggregate size distribution is the same as that in Chapter 6 and the volume of aggregate is 39.6%. The simulation is conducted by displacement control on the top and bottom boundaries and load control on the side boundaries as shown in **Fig. 34.** Loads of the side boundaries are applied until the target values and are then kept constant while the displacement on the top and bottom boundaries is increased until complete failure occurs. Friction between specimen and loading boundaries is eliminated. The target compressive strength of mortar is 35 MPa. To obtain the failure criterion under biaxial stress condition, compression and tension analyses where the applied load on the side

boundaries are different are conducted.

7.1 Compression-tension test and tension-tension test

The normalized predicted stress states at failure are shown in **Fig. 35** under compression-tension and tension-tension loading conditions. In the analysis, uniaxial compressive and tensile strengths are 25.43 MPa and 2.43 MPa, respectively. The curve in **Fig. 35** presents the failure criterion of the Niwa model in the compression-tension domain and the Aoyagi-Yamada model in the tension-tension domain (Aoyagi and Yamada 1983, Niwa et al. 1987). Experimental data obtained by Kupfer et al. (1969) are also indicated. In the compression-tension domain, the analysis results show stress states at failure that are similar to the criterion models and experimental results to some extent. In the tension-tension domain, the analytical results do not agree with the Aoyagi-Yamada model. However in the criterion for tension-tension domain developed by Kupfer and Gerstle (1973), the value is a constant that is the uniaxial tensile strength. The stress states in Kupfer's experimental results in tension-tension domain are well simulated by the analysis.

Figure 36 a) - d) show the crack pattern of specimens whose failure stress states are A-D in **Fig. 35.** Cracks whose widths reach 0.005 mm in **Fig. 36 a)** and **b)** and 0.002 mm in **Fig. 36 c)** and **d)** when the stress at the displacement control boundary declines to approximately 65% of the peak stress in the post-peak process are presented. In the uniaxial compression test, a diagonal crack is formed at approximately 30 degrees in relation to the loading direction (**Fig. 36 a)**). By applying the tensile stress on the lateral side, crack angles become fairly parallel to the compression load axis (**Fig. 36 b)**). **Figure 36 c)** shows the crack pattern of the uniaxial tension test in which propagation of a single crack is simulated. In the biaxial tension test, cracks are not localized but rather distributed in the specimen (**Fig. 36 d)**). These changes in crack pattern are the same as those observed in the experiment by Kupfer et al (1969), except for the fact that the experimental results show rather localized cracks.

7.2 Compression-compression test

The RBSM analysis developed in this study cannot simulate the biaxial compression failure because cracks in the normal direction to the plane of the specimen, which is the primary cause of failure under biaxial compression, cannot be represented. The displacement condition in two-dimensional analysis is in a sense the same as the condition in three-dimensional analysis where displacement in the third direction is restricted. **Figure 37** shows the stress strain relations in the longitudinal direction of specimens in the two-dimensional analysis of compression-compression tests. Stress in the lateral direction is kept as confinement stress. The predicted curves show a significant increase in peak stress

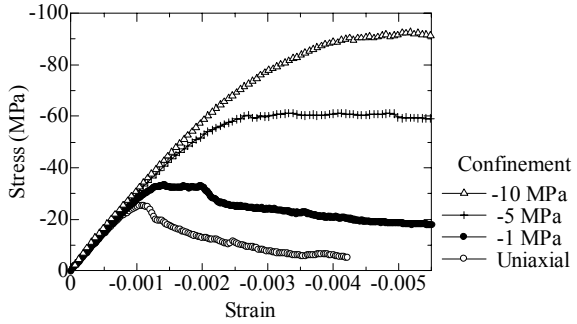

Fig. 37 Biaxial compression test.

with the confinement stress. This fact and the shapes of the stress strain curves are similar to the usual experimental results of triaxial compression tests of concrete (Chen 1982).

8. Conclusions

The following conclusions are drawn from the analyses of mortar and concrete using the two-dimensional Rigid Body Spring Model (RBSM) with meso scale elements, where only tension and shear failure of springs and no compression failure is assumed.

(1) In compression tests of mortar, macroscopic compressive strength is well predicted by meso scale analysis. The calculated stress strain curve shows a similar shape to that in usual experimental results.
(2) In compression tests of concrete, the predicted stress strain curve and changes in Poisson's ratio are similar to those in experiments. A sudden increase in the number of cracks in meso scale before the peak stress can be predicted. Different crack patterns due to the different loading boundary conditions can be simulated reasonably well.
(3) Reduction in macro compressive and tensile strengths of the concrete due to the inclusion of aggregates can be predicted.
(4) The analysis predicts well the compressive and tensile strength relationship of mortar and concrete.
(5) Variations in the strength of mortar and concrete are not much larger than those observed in experiments.
(6) In the tension analysis of the mortar and concrete, the localization of failure after the peak stress and the propagation of a single crack can be simulated.
(7) As observed in experiments, the localized compressive failure zone and unloading zone are predicted in the compression test of the specimens whose dimensions in the loading direction are 400 and 600 mm by the analysis. However, the localized compressive failure zone is predicted to be larger than that in experiments.
(8) The analysis can reasonably simulate the failure criterion under biaxial stress condition in the compression-tension and tension-tension domains.
(9) The predicted stress strain curve in the biaxial compression test is similar to that obtained in the triaxial

compression test in experiments.

References

Aoyagi, Y. and Yamada, K. (1983). "Strength of deformation characteristics of reinforced concrete shell elements subjected to in-plane force." *Proceeding of JSCE*, 331,167-180. (in Japanese)

Asai, M., Terada, K., Ikeda, K., Suyama, H. and Fujii, K. (2003). "Meso-scopic numerical analysis of concrete structure by a modified lattice model." *J. Struct. Mech. Earthquake Eng.*, JSCE, 731, 19-30.

Bazant, Z. P., Caner, F. C., Cedolin, L., Gusatis, G. and Di Luzio, G. (2004). "Fracturing material models based on micromechanical concepts." *Proceedings of FraMCoS-5*, 83-89.

Bolander, J. E. and Saito, S. (1998). "Fracture analysis using spring network models with random geometry." *Engineering Fracture Mechanics*, 61, 569-591.

Chen, W. F. (1982). "Plasticity in reinforced concrete." New York: McGraw-Hill Book Company.

Christensen, P. N. and Nielsen, T. P. H. (1969). "Modal deformation of the effect of bond between coarse aggregate and mortar on the compressive strength of concrete." *ACI Journal*, 66(1), 69-72.

Cundall, P. A. and Strack, O. D. L. (1979). "A discrete numerical model for granular subassemblies." *Geotechnique*, 29, 47-65.

Goble, C. F. and Cohen, M. D. (1999). "Influence of aggregate surface area on mechanical properties of mortar." *ACI Materials Journal*, 96 (6), 657-662.

Gopalaratnam, V. S. and Shah, S. P. (1985). "Softening response of plain concrete in direct tension." *ACI Journal*, 82 (3), 310-323.

Harsh, S., Shen, Z. and Darwin, D. (1990). "Strain-rate sensitive behavior of cement paste and mortar in compression." *ACI Materials Journal*, 87 (5), 508-516.

Hsu, T. T. C. and Slate, F. O. (1963). "Tensile bond strength between aggregate and cement paste or mortar." *Journal of ACI*, 60 (4), 465-485.

JSCE, (2002a). "*Standard specification for concrete structures, Materials and construction*." Tokyo: Japan Society of Engineers, (in Japanese)

JSCE, (2002b). "*Standard specification for concrete structures, Structural performance verification*." Tokyo: Japan Society of Engineers, (in Japanese)

Kato, K. (1971). "Microcracks and physical properties of plane concrete." *Proceedings of JSCE*, 188, 61-72. (in Japanese)

Kawai, T., (1977). "New element models in discrete structural analysis." *Journal of the Society of Naval Architects of Japan*, 141, 187-193.

Kawai, T. and Takeuchi, N., (1990)."*Discrete limit analysis program, Series of limit analysis by computer 2*." Tokyo: Baifukan. (in Japanese)

Kosaka, Y. and Tanigawa, H. (1969). "Study on influence of size of specimen and friction of loading surface on compressive strength of various concrete." *Cement Concrete*, 265, 2-10. (in Japanese)

Kosaka, Y. and Tanigawa, Y. (1975a). "Effect of coarse aggregate on fracture of concrete (part 3)." *Journal of AIJ*, 233, 21-32. (in Japanese)

Kosaka, Y. and Tanigawa, Y. (1975b). "Effect of coarse aggregate on fracture of concrete (part 2)." *Journal of AIJ*, 231, 1-11. (in Japanese)

Kosaka, Y., Tanigawa, Y. and Kawakami, M. (1975). "Effect of coarse aggregate on fracture of concrete (part 1)." *Journal of AIJ*, 228, 1-11. (in Japanese)

Kotsovos, M. D. (1983). "Effect of testing techniques on the post-ultimate behavior of concrete in compression." *Materials and Structures*, 16 (91), 3-12.

Kupfer, H. B. and Gerstle, K. H. (1973). "Behavior of concrete under biaxial stresses." *Proceeding of ASCE*, 99(EM4), 853-866.

Kupfer, H., Hilsdorf, H., K. and Rusch, H. (1969). "Behavior of concrete under biaxial stresses." *ACI Journal*, 66(8), 656-666

Markeset, G. and Hillerborg, A. (1995). "Softening of concrete in compression localization and size effects." *Cement and Concrete Research*, 25 (4), 702-708.

Matsushita, H., Tsuruta, H. and SUE, Y. (1999) "Effect due to friction of loading surface on the uniaxial compression test", *Cement Science and Concrete Technology*, 53, 621-626. (in Japanese)

Nagai, G., Yamada, T. and Wada, A. (1998). "On a finite element procedure based on real 3-dimensional image for concrete materials." *J. Struct. Constr. Eng.*, AIJ, 509, 77-82. (in Japanese)

Nagai, K. (2002). "*Numerical simulation of fracture process of concrete model by Rigid Body Spring Method*." Thesis (Master of Eng.). Hokkaido University.

Nagai, K., Sato, Y. and Ueda, T. (2002) "Numerical simulation of fracture process of plain concrete by Rigid Body Spring Method." *Proceedings of the first fib Congress 2002 Concrete Structures in the 21st Century*, 8, 99-106.

Nagai, K., Sato, Y. and Ueda, T. (2004). "Three-dimensional meso-scopic analyses of mortar and concrete model by Rigid Body Spring Model. " *Proceedings of FraMCoS-5*, 353-360.

Nagamatsu, S. (1976). "Statistical properties of mortar and concrete strength." *Journal of AIJ*, 240, 9-19. (in Japanese)

Niwa, J., Yamada, K., Yokozawa, K. and Okamura, H. (1987). "Revaluation of the equation for shear strength of reinforced concrete beams without web reinforcement." *Concrete Library of JSCE*, 9, 65-84.

Stroeven, P. and Stroeven, M. (2001). "Space approach to concrete's space structure and its mechanical properties." *Heron*, 46 (4), 265-289.

Stock, A. F., Hannant, D. J. and Williams, R. I. T. (1979). "The effect of aggregate concentration upon the strength and modulus of elasticity of concrete."

Magazine of concrete research, 31 (109), 225-234.

Sugihara, K. (1998). "*Fortran Computational Geometry Programming*." Tokyo: Iwanami Shoten. (in Japanese)

Suzuki, S., Masuda, Y. and Nakamura, N. (2003). "Study on probability distribution of compressive strength of concrete (part 1)*." Summaries of technical papers of annual meeting AIJ conference 2003 A-1*, 715-716. (in Japanese)

Taylor, M. A. and Broms, B. B. (1964). "Shear bond strength between coarse aggregate and cement paste or mortar." *Journal of the ACI*, 61 (8), 939-956.

Trende, U. and Buyukozturk, O. (1998). "Size effect of aggregate roughness in interface fracture of concrete composites." *ACI Materials Journal*, 95 (4), 331-338.

Ueda, M., Hasebe, N., Sato, M. and Okuda, H. (1993). "Fracture mechanism of plain concrete under uniaxial tension." *J. Materials, Conc. Struct., Pavements*, 19, 69-78. (in Japanese)

Ueda, M., Kei, T. and Taniguchi, H. (1988). "Discrete limit analysis of reinforced concrete structures by RBSM." *Proceedings of JCI*, 10 (3), 335-338. (in Japanese)

Ueda, T., Hasan, M., Nagai, K. and Sato, Y. (2004). "Stress-strain relationship of concrete damaged by freezing and thawing cycles." *Proceedings of FraMCoS-5*, 645-652.

van Mier, J. G. M. (1986). "Multiaxial strain-softening of concrete." *Materials and Structures*, 19 (111), 179-200.

Watanabe, K., Niwa, J., Yokota, H. and Iwanami, M. (2003). "Formulation of stress-strain relationship of concrete considering localized compressive failure zone." *J. Materials, Conc. Struct., Pavements*, 725,197-211. (in Japanese)

Wittmann, F. H. (2004). "Crack formation and life cycle performance." *Proceedings of FraMCoS-5*, 3-10.

Yokomichi, H., Kakuta, Y. and Terasawa, S. (1970). "Significant point and fracture in deformation of concrete." *Proceedings of Technique on Cement*, XXIV, 282-285. (in Japanese)

Yoshimoto, A., Hasegawa, H. and Kawakami M. (1983). "Comparison of strength obtained from pure tension, split and bending tests of concrete and mortar." *Cement Concrete*, 435, 42-48. (in Japanese)